SAND2022-11959C

Proceedings of 2022 Hypervelocity Impact Symposium
HVIS2022
September 18-22, 2022, Alexandria, VA, USA

HVIS2022-####

ULTRA-HIGH-G BALLISTIC IMPACT INTO WATER TARGETS

Natasha Wilson[1], Caleb White[1], Alex Chen[1], Shane Curtis[1], Don Lifke[1]

[1]Sandia National Laboratories, Albuquerque, NM

ABSTRACT

Creation of a Sandia internally developed, shock-hardened Recoverable Data Recorder (RDR) necessitated experimentation by ballistically-firing the device into water targets at velocities up to 5,000 ft/s. The resultant mechanical environments were very severe—routinely achieving peak accelerations in excess of 200 kG and changes in pseudo-velocity greater than 38,000 inch/s. High-quality projectile deceleration datasets were obtained though high-speed imaging during the impact events. The datasets were then used to calibrate and validate computational models in both CTH and EPIC. Hydrodynamic stability in these environments was confirmed to differ from aerodynamic stability; projectile stability is maintained through a phenomenon known as "tail-slapping" or impingement of the rear of the projectile on the cavitation vapor-water interface which envelopes the projectile. As the projectile slows the predominate forces undergo a transition which is outside the codes' capabilities to calculate accurately, however, CTH and EPIC both predict the projectile trajectory well in the initial hypervelocity regime. Stable projectile designs and the achievable acceleration space are explored through a large parameter sweep of CTH simulations. Front face chamfer angle has the largest influence on stability with low angles being more stable.

Keywords: shock testing, water impact, ultra-high-G, ballistics, incremental Latin hypercube sampling, extreme environment

NOMENCLATURE

ΔV_p	PVSS pseudo-velocity asymptote
A_0	PVSS acceleration asymptote

1. INTRODUCTION

Current sub- and full- scale environmental testing methods for high-G applications are expensive and time consuming. Using these methods, design flaws are often revealed only after significant development funding has been exhausted. If alternative test methods could be used earlier in the design process (before full-scale testing ensues) to verify and qualify designs, there would be more time and funding to implement required corrections. While lab-scale testing can locate some issues early in development, the limited range of achievable environments restricts the type of exposable flaws and thus there exists a gap between lab-scale and full-scale testing methods.

For example, the capabilities of various lab-scale and sub-scale test methods are plotted in terms of maximum achievable acceleration versus pulse duration in Figure 1 (reproduced from [1]). Lab-scale test methods include a Hopkinson Bar [2] [3], Very High G (VHG) Machine [4], and a classic Drop Tower (example drop tower [5]). As shown, there is some overlap, but there are large swaths of the spectra (g-level vs time) that are not currently covered by cost effective testing methods.

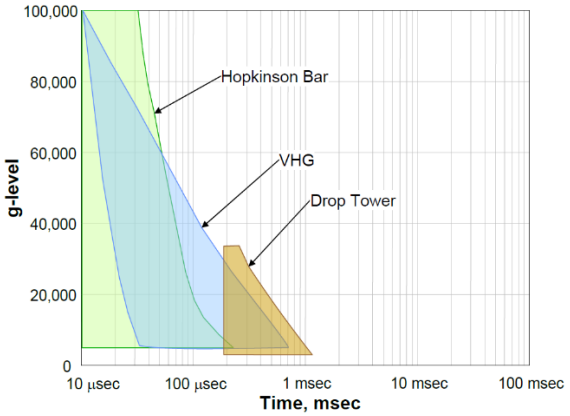

FIGURE 1: ACCELERATION LEVEL VS. PULSE DURATION FOR DIFFERENT HIGH-G TEST METHODS MODIFIED FROM [1]

A new sub-scale test method, which we have coined as Ballistic Water Impact (BWI), has the potential to bridge the gap between lab- and full- scale acceleration environments for high-G applications. BWI is simple in theory—it involves shooting a

test article into a water target. This type of testing has been utilized in the development of a Sandia National Laboratories (SNL) internally developed, Recoverable Data Recorder (RDR) [6] [7]. In that program, operational requirements for the RDR necessitated extreme environment experimentation wherein a projectile was shot into a water target at impact velocities up to 5,000 ft/s. The water targets were either "disposable" or "reusable", as shown in Figure 2 and Figure 3, respectively. The disposable target test series was performed at the Energetic Materials Research and Test Center (EMRTC) in Socorro, NM. That experimental setup was very minimalistic and inexpensive with the only required equipment being: 1) a medium-bore gun, 2) a disposable tank composed of plywood and a sheet of polycarbonate, 3) a soft backstop, and 4) a safe firing location. Bulk deceleration of the projectile was obtained using high-speed video cameras that tracked the Unit-Under-Test as it decelerated in the water target. The reusable target was built at Kirtland Air Force Base in Albuquerque, NM. While the reusable tank was more expensive, it did have some logistical advantages including better high-speed video. Regardless, BWI testing is possible with either type of target. Based on the deceleration results from the RDR development testing, it was hypothesized that BWI testing could offer a repeatable, inexpensive sub-scale test method that can bridge the gap to full-scale tests earlier in the design process for high G applications.

FIGURE 2: BWI USING DISPOSABLE WATER TANKS [6]

FIGURE 3: BWI REUSABLE WATER TANK [6]

The RDR testing provided initial insight into the possibilities of BWI testing but did not explore the full range of possibilities. The goal of the current work was to better understand the potential of the BWI testing space. At a high level, a multidimensional parameter sweep was performed using simulation tools to map input parameters (e.g., impact velocity, mass, frontal area, projectile dimensions, etc.) to the resultant mechanical environments to drive future design decisions when testing to a desired impact environment.

2. MATERIALS AND METHODS

Simulation of the BWI projectiles traveling through a block of water was performed using CTH to obtain displacement and velocity through time. Dimension and velocity ranges were chosen based on the disposable tank RDR testing and engineering judgement. To minimize the number of simulations required, while still thoroughly covering the range of selected parameters, incremental Latin Hypercube Sampling was used. Position and velocity data was differentiated to obtain acceleration, filtered to remove high-frequency content, and fit with an equally damaging haversine pulse. The haversine pulse was used to determine the amplitude and duration of the acceleration encountered by each projectile.

2.1 RDR testing tanks

RDR testing was performed in two different styles of tanks, a large steel reusable tank and smaller disposable tanks. The disposable tanks were created with a sheet of plywood (4'x8'), polycarbonate sheet (4'x8'x3/4"), polystyrene foam sheet (1.5'x1.5'), screws, and silicone. To build each disposable tank costs on the order of $500 for materials, making this approach a less expensive alternative to reusable tank testing. The simulations have the same dimensions as those in the disposable tank tests.

Projectiles were shot at speeds up to 5,000 ft/s into the water targets. In the case of the disposable tanks, the projectile was captured in a soft catch after exiting the water.

2.2 Hydrodynamic simulations

The water impact events for the parameter space mapping are simulated with CTH [8]. Dakota [9] was used to conduct all the simulations in parallel on SNL's High Performance Computing platforms. The sampling method selected to ensure the entire space is sampled with equal density was the incremental Latin Hypercube Sampling (iLHS).

CTH is a multidimensional, multi-material, large deformation, strong shock, solid mechanics code (also known as a hydrocode) developed at SNL [8]. The numerical solver in CTH consists of a two-part solution scheme—a Lagrangian distortion step during which the mesh deforms to follow the material motion and a Eulerian remap step during which the distorted mesh is mapped back onto the original mesh. The conservation of volume, mass, momentum, and energy equations are approximated using explicit finite-volume schemes [10].

Simulations on the RDR test conditions showed good agreement between the simulated and measured results. Good agreement was also shown between EPIC simulations (a

Lagrangian dynamics hydrocode operated by the Southwest Research Institute) and the measured results.

CTH predictions were performed by inserting generic projectiles (created in Cubit [11]) into a two-dimensional, rectangular domain. The quality of the projectile conformal mesh from a finite-element standpoint is of no concern, only that the material surfaces be smoothly represented. The projectile was given the steel SESAME equation of state along with the 4340 steel Johnson-Cook viscoplastic and fracture models. The Tillotson equation of state was used for water. All the material constants are included in the CTH library.

The water targets were modeled after the disposable water tanks used at the EMRTC RDR test (i.e., 8x2x2 feet) [7]. Outflow/vacuum boundary conditions (zero pressure in ghost cells) were placed on all sides of the spatial domain (which was slightly larger than the water tank) to allow the water to leave during penetration and not interfere with the projectile similar to the disposable tank RDR setup. The resolution of the Eulerian mesh is controlled via adaptive mesh refinement. The refinement criteria are such that the projectile is kept at maximum refinement while the remainder of the mesh is refined upon density differences (i.e. interfaces). Eight refinement levels are prescribed which allow a minimum refinement cell size of 0.0342 cm. Tracers are located at the tip and tail of the projectile along the center axis.

2.3 Projectile definition and parameters

Selecting the frontal geometry of the projectiles for simulation was aided by the stability lessons learned in early RDR testing which used projectiles fired into water targets to assess component survivability. Early RDR projectiles possessed an ogive profile which greatly reduces drag in aerodynamic applications, however, it was discovered that the ogive profile is highly unstable in hydrodynamic penetration environments [6].

A lesser-known stability method in literature for projectiles undergoing supercavitation—a phenomenon where the projectile is fully encased in a cavitation bubble resulting in only the projectile's nose being wetted thereby created a low-drag environment [12, 13, 14, 15]—is impingement (or *tail-slapping*, depicted in Figure 4) of the projectile's tail on the liquid-vapor interface of the cavitation bubble.

Flat (or blunt) frontal nose shapes have been shown to produce the largest cavitation bubble and to be the most stable at high velocities [12]. Thus, the shape of the projectile nose and length over diameter ratio should be designed such that the resulting cavitation bubble encases the full length of the projectile. However there exists an engineering trade-off: namely, the larger the frontal surface area the greater the acceleration loads experienced by the projectile. One solution is to design a tip which tapers down to a flat surface—a trapezoidal cross-sectional area. This is the shape chosen for the BWI study.

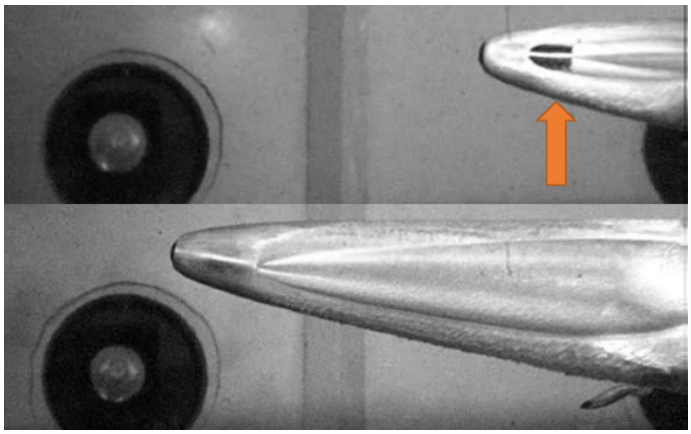

FIGURE 4: TAIL-SLAPPING IN RDR TESTING [7]

The parameter space variables were chosen to be impact velocity, projectile length, projectile diameter, chamfer diameter (via the diameter ratio), and chamfer angle which are depicted in Figure 5. There are other variables which could be perturbed (i.e., the length of the disposable tank or a tank medium other than water), however, that is outside the scope of this study and is left for future work. Projectile mass is a variable of interest; however, it is calculated though the projectile density and dimensions rather than being directly prescribed. Diameter ratio is defined as the chamfer diameter divided by the projectile diameter. This prevents unrealistic situations where the chamfer diameter is greater than the projectile diameter.

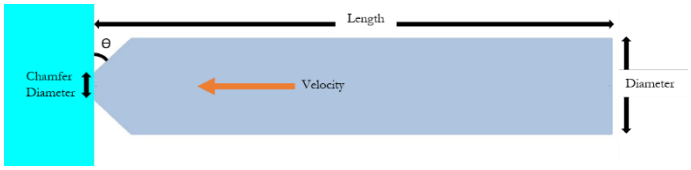

FIGURE 5: GENERIC PROJECTILE DIMENSIONS

The bounds of the parameter space were chosen to circumscribe a reasonable, physical domain of interest. A gun's bore diameter restricts the mechanical envelope of a projectile, so the upper limit on the projectile diameter range was chosen based on the gun used at EMRTC for the RDR project. Larger gun bores exist, and the corresponding larger projectile sizes may be examined in future works. The bounds of the parameter space are given in Table 1.

TABLE 1: PARAMETER SPACE BOUNDS

Parameter	Minimum	Maximum
Velocity	500 ft/s	5,000 ft/s
Length	1 inch	6 inch
Diameter	0.5 inch	1.5 inch
Diameter Ratio	0.2	0.8
Chamfer Angle	0°	60°

2.4 Incremental Latin hypercube sampling

Latin Hypercube Sampling (LHS) is a pseudo-random, stratified technique that divides the cumulative distribution for each variable into n non-overlapping, intervals of equal probability [16, 17]. A Latin Hypercube is the generalization of a Latin Square—a square grid is a Latin Square if and only if there is only one sample in each row and column—into an arbitrary number of dimensions. Similarly, LHS is a k-dimensional extension of Latin Square sampling. Incremental Latin Hypercube Sampling (iLHS) enables further sampling to be performed until convergence is reached. Each incremental sample doubles the total number of samples and contains the results of the previous hypercubes. The full sample is itself a Latin Hypercube—the stratification and correlation structure are maintained [16].

It is difficult to make a rigorous convergence assertion using random Monte Carlo sampling techniques. Because of the random sampling, previous samples are not considered when incrementing the random samples. The assumption cannot be made that the sample set has filled the probability space, nor that the entire space has been sampled with sufficient density. It typically takes orders of magnitude more samples to achieve convergence with random Monte Carlo than with iLHS.

2.5 Quantities of interest and post processing

The quantities of interest are:

- Maximum change in Pseudo-Velocity (ΔV_p) from the Pseudo-Velocity Shock Response Spectra (PVSS).
- Peak and duration of the acceleration pulse.
- Projectile Angle of Tilt (AoT) with respect to the horizontal—the angle between the projectile axis and the x-axis.

The maximum change in pseudo-velocity, and the acceleration peak and duration are both metrics of "damage"—albeit the acceleration peak and duration are not the best "damage" metrics but is the primary metric in literature—and used to quantitatively characterize the severity of a shock for comparison purposes. The projectile AoT is considered as a measure of instability—certain permutations of the input parameters result in a projectile that is unable to maintain a stable trajectory through the length of the tank.

The datasets for all simulations are post-processed using Python. CTH outputs temporal displacement and velocity datasets, of which velocity is differentiated to obtain acceleration, and acceleration is differentiated to obtain jerk. The datasets are differentiated by interpolating the original dataset with a piecewise cubic polynomial (i.e., cubic spline interpolation) which (the polynomial) is then differentiated and evaluated at the discretized temporal locations. The displacement, velocity, acceleration, jerk, and AoT time-histories, as well as the acceleration and pseudo-velocity maxima shock response spectra (SRS), are shown for all simulations.

The digital signal processing (DSP) methodology occurs as follows.

1. The datasets are regularized though cubic spline interpolation to ensure a constant timestep between the data points.
2. The datasets are then pre- and post- extended to encourage proper edge behavior when filtering. The velocity datasets are pre-extended with the initial velocity and post-extended with the mean of a set number of previous values (high-frequency content near the end necessitated this as some datasets would sharply increase in velocity in the post-extend region).
3. The simulation datasets are then decimated with anti-aliasing protection—an 8th order, lowpass, bi-directional, Butterworth infinite impulse response (IIR) filter—from their original sample-rates ($f_s \approx 1$ MHz) to a decimation sample-rate of f_d = 250 kHz to enable greater accuracy in temporal peak amplitude estimation (within 95% accuracy if sample rate is 10*f_c).
4. The acceleration datasets are obtained through differentiation as noted above.
5. The acceleration datasets are then filtered with a 6th order, lowpass, bi-directional, Butterworth IIR filter with a cutoff frequency of f_c = 10 kHz. The cutoff frequency was chosen with engineering judgement through examination of the acceleration Discrete Fourier Series spectrums.
6. The post-extend regions of the acceleration datasets are removed prior to computing the maximax acceleration and pseudo-velocity SRS—a light damping value of ζ = 5% is assumed.

The shock response spectrum yields the peak response of a hypothetical single degree of freedom system (e.g., simple spring-mass-damper) to a transient acceleration input across a spectrum of natural frequencies. The SRS is non-unique and is used both to compare acceleration inputs and as a metric for shock severity—peak, temporal acceleration levels alone do not exhibit a straightforward correlation to shock-induced damage

[18]. The pseudo-velocity SRS (PVSS) is particularly insightful as peak model stress is proportional to the change in pseudo-velocity [18, 19]. The PVSS is displayed on a tripartite plot wherein the displacement and acceleration are given through logarithmic, diagonal axes (±45° slopes) in addition to the pseudo-velocity and natural frequency axes. The PVSS is plotted over the frequency domain, thus revealing more information than just the acceleration plotted over time. Shocks that yield a pseudo velocity change on the order of ΔV_p = 200–500 inch/s are often considered very severe [18].

Calculating the duration of an acceleration pulse is non-trivial; a variety of methods exist in literature with varying degrees of success. Popular methods include: a) taking the delta between the rising and falling edge at a threshold of 90% of the peak amplitude, and b) fitting a quadratic to the peak amplitude and slopes of the rising and falling edges, then taking the delta between the 90% peak threshold [20]. However, these methods lose robustness with acceleration pulses that fail to cross the 90% peak threshold or that possess a high degree of skewness (i.e., sharp rising edge and gradual falling edge). Another (and perhaps superior) method involves calculating a representative, idealized haversine pulse (which is characterized by a magnitude and duration) from the PVSS of the acceleration pulse [19]. The PVSS, by formulation, is non-unique and is a measure of damage. Therefore, if two different acceleration pulses produce an equal (similar) PVSS, then they can be considered equally damaging over a certain natural frequency range. These impact simulations generate heavily skewed acceleration profiles, thus the haversine pulse calculated from the PVSS is selected to represent the acceleration duration. The duration, T, of the idealized haversine pulse can be calculated from the acceleration PVSS as follows:

$$\Delta V_p = \int_0^T \frac{A_0}{2}\left[1 - \cos\left(\frac{2\pi t}{T}\right)\right]dt = \frac{A_0\ T}{2} \qquad (1)$$

Where ΔV_p and A_0 are the PVSS pseudo-velocity and acceleration asymptotes, respectively. This yields a representative, idealized haversine pulse that is similarly as damaging as the acceleration pulse and is characterized by definitive magnitude and duration values.

3. RESULTS AND DISCUSSION

The RDR test articles achieved peak accelerations in excess of 200 kG and changes in pseudo-velocity greater than 38,000 inch/s. Tail-slapping was also observed during the RDR tests (Figure 4).

With the total number of simulations doubling at each iLHS refinement, the first refinement ran five more simulations (for a total of 10), the second refinement ran 10 more simulations (for a total of 20), the third refinement ran 20 more simulations (for a total of 40), and so on. The iLHS refinements resulted in a total of 640 completed simulations with parameter values spanning the parameter ranges (Table 1).

3.1 Projectile stability

An example of one of the hydrodynamically stable simulations is shown in Figure 6 (top) with a white cavitation bubble. Some simulations resulted in projectiles that were hydrodynamically unstable and thus tumbled or sharply veered from the initial x-direction path. One of these simulations is pictured in Figure 6 (bottom) with the projectile beginning to tumble. The shapes of the stable and unstable projectiles are also included in the figure.

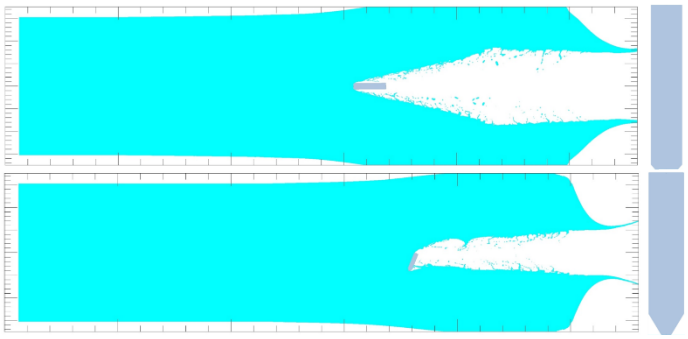

FIGURE 6: STABLE (TOP) AND UNSTABLE (BOTTOM) PROJECTILE CTH SIMULATION

The AoT of each projectile was tracked through each simulation and the maximum AoT was returned. A maximum AoT of greater than or equal to 45° was used as the criteria for an unstable projectile. This was chosen as the cutoff because even if the projectile returned to fly straight after an AoT greater than 45°, the acceleration profile would likely be undesirable.

3.2 Example simulations

As an example of a stable projectile starting at a high velocity, a projectile was simulated with length 4.48 in, diameter 0.74 in, diameter ratio 0.446, and chamfer angle 4.36°. The high diameter ratio and small chamfer angle gives the projectile a very blunt front face (Figure 7).

While the projectile almost immediately started to tilt after entering the water, the tilt never exceeded 16° (Figure 7). Less than one full oscillation about level (0° tilt) was observed before the simulation ended when the projectile exited the water. In this simulation, the projectile's decrease in angle of tilt was due to the projectile self-stabilizing using the tail slapping method. As the projectile tilted farther, the back end (at 3.95 seconds) hit the edge of the vapor cavity and reversed the tilt.

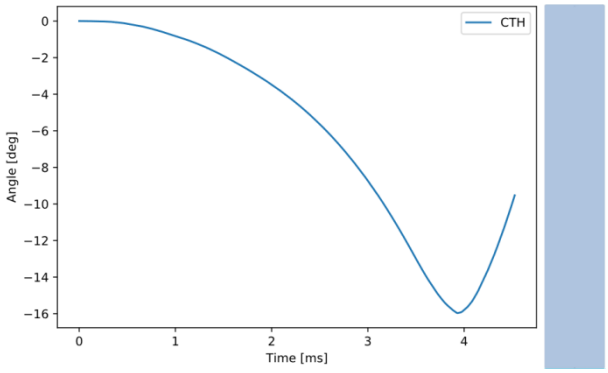

FIGURE 7: ANGLE OF TILT AS A FUNCTION OF TIME WITH THE CORRESPONDING PROJECTILE.

This simulation has a clean displacement profile with a gradual decrease in slope (decreased velocity) with time (Figure 8 a & b, velocity with 10 kHz filtering). Acceleration and jerk plots show that the velocity and acceleration change the most when the projectile first impacts the water as is expected (Figure 8 c & d, negative values indicating a decrease in velocity or acceleration). Both plots show smaller spikes at the end of the data beginning approximately when the projectile tail hit the edge of the cavitation bubble.

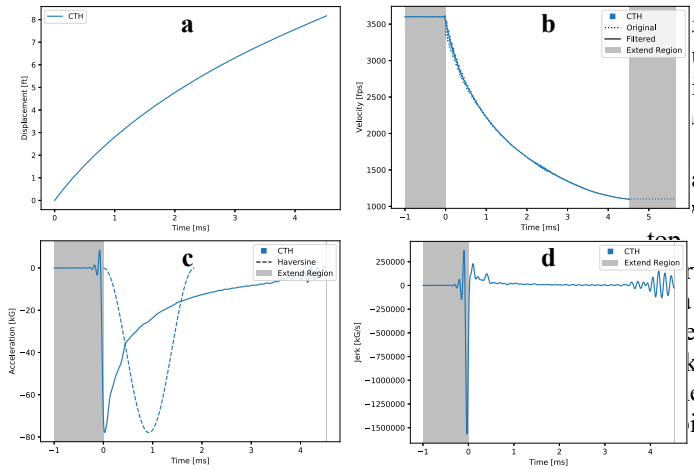

FIGURE 8: POSITION (A), VELOCITY (B), ACCELERATION (C), AND JERK (D) PLOTS.

The acceleration returns to zero at the end of the simulation when the projectile exits the water but takes the entire simulation to gradually reach zero. A slow reduction in acceleration combined with the sharp initial acceleration at impact creates an asymmetric acceleration pulse (Figure 8 c). When the acceleration data is plotted with its natural frequency components (acceleration response spectra) the effect of the acceleration pulse's asymmetry is seen (Figure 9 a). The PVSS also shows deviation from a symmetric pulse (Figure 9 b). When the fitted Haversine pulse is plotted on top of the acceleration data, the peak acceleration matches but the width of the pulse appears somewhat wider than the initial CTH acceleration spike (Figure 8 c). The long trailing edge of the acceleration increases the width of the asymmetric acceleration pulse requiring the wider Haversine pulse to obtain a hypothesized equally damaging profile.

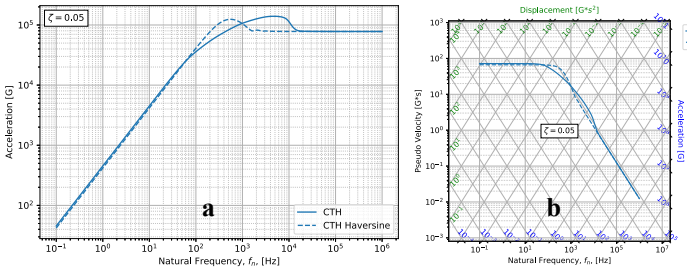

FIGURE 9: ACCELERATION RESPONSE SPECTRA (A) AND PVSS (B) PLOTS

3.3 Testing space mapping

The calculated acceleration and spike duration for each ulation were plotted to show the range of testing space ure 10, x axis is log scaled). Most acceleration/duration pairs into a band that tends towards smaller accelerations as the tion increases.

Simulations with high accelerations were almost all able. The distribution of stable and unstable projectiles is vn in Figure 10 with the predominantly unstable region at the This cluster of unstable projectiles at high accelerations and t durations could be due to the increase in wetted surface rapidly decreasing its velocity as the projectile angle of tilt eeds 45°. While most of the stable simulations have lower k accelerations there are still unstable projectiles covering the e range, so acceleration level alone is insufficient to predict ility.

The BWI simulation acceleration vs duration results (stable and unstable results included) are compared in Figure 11 to the other testing methods. This comparison shows how the BWI method spans a large region not covered by other sub-scale tests. Unlike the other testing method ranges shown in the figure, the BWI testing method range includes a large region of high-G and high duration. Since achieving both high-G and long duration

times is difficult, a testing method that can achieve both is valuable.

Considering only the stable projectiles, all simulations had changes in pseudo velocity indicating a very severe shock. As the projectile's starting velocity increases so does the maximum pseudo velocity. At a similar starting velocity, the pseudo velocity maximum is lower for an unstable projectile compared to a stable projectile.

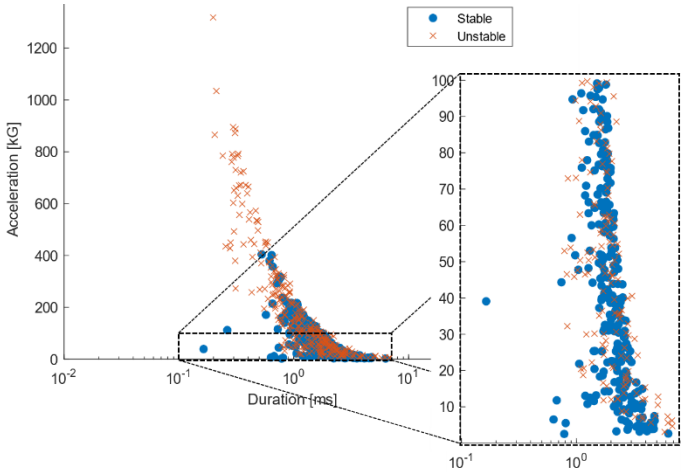

FIGURE 10: PEAK ACCELERATIONS AND DURATIONS FOR EACH PROJECTILE CLASSIFIED BY STABILITY.

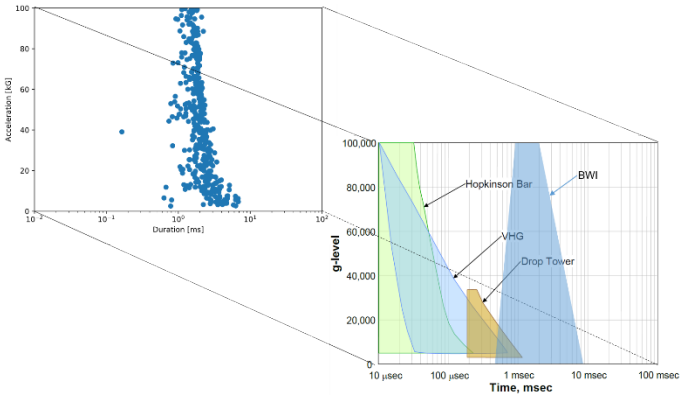

FIGURE 11: BWI TESTING METHOD COMPARISON WITH OTHER TESTING METHODS (RIGHT IMAGE MODIFIED FROM [1]).

3.4 Input variables' relationships with stability

To observe input variables' influence on stability, a Bootstrap Forest model was used. A bootstrap sample is a random sample of observations, drawn with replacement from the data. This can be used to create multiple sampled sets from the main dataset. Decision tree models are created for each of these sampled sets (with the input variables also sampled at each split in the decision tree) and then these decision trees are averaged together to form a Bootstrap Forest model [21]. This is useful when weaker input factors are overpowered by stronger contributors, often due to a strong correlation between the weak and strong factors. It allows the weaker contributors to be included in the model which can produce a more powerful model. This analysis method was used on the simulation input parameters to determine which parameters and parameter combinations affect the stability of a projectile. The resulting model accurately predicted the stability of 618 (out of the total 640) projectiles.

Chamfer angle was inversely related to stability with low angles being much more stable than high angles. At low chamfer angles (<15°), the only other input parameter that had a large impact on stability was the length of the projectile with longer projectiles being more stable. For medium chamfer angles (20-30°), increased length and increased diameter ratio have a positive effect on stability. Once high chamfer angles are reached (>30°) the projectile will be unstable with only the diameter ratio somewhat increasing the stability. A projectile with a small diameter ratio and high chamfer angle would resemble an ogive shape nose which is not hydrodynamically stable (as discussed previously). While increasing the diameter ratio on a highly chamfered projectile would provide more of a flat front face to help with stability, the ratio must be at the highest end of the range to overcome the destabilizing effect of a high chamfer angle. There is also interaction between chamfer angle and diameter ratio with large diameter ratios stable across all chamfer angles, but small diameter ratios require small chamfer angles to maintain stability.

Another Bootstrap Forest model was applied to the stable projectiles to determine what inputs most affected the peak acceleration. Of the input variables, velocity was the most significant predictor of peak acceleration.

A summary of the four major stability trends is shown in Figure 12. Stability is more likely for low chamfer angles, increased length when chamfer is low, increased length when chamfer is moderate, and increased diameter ratio when chamfer angle is high.

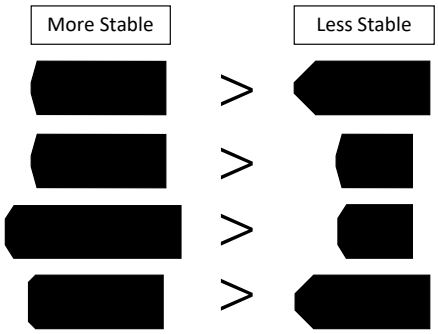

FIGURE 12: PROJECTILES MORE AND LESS LIKELY TO BE STABLE

4. CONCLUSION

Low chamfer angles have the largest effect in creating a stable projectile in the regime studied. In stable projectiles, velocity is the input that controls the peak acceleration where lower velocity corresponds to a lower peak acceleration.

ACKNOWLEDGEMENTS

Thanks to John Korbin for helping develop the CTH model and Gilbert Archuleta for financial management at SNL. This project was funded through the Department of Defense Office of the Secretary of Defense Joint Enhanced Munitions Technology Program, formerly the Joint Fuze Technology Program, project 21-G-014. Some of the experimental work was leveraged from SNL Lab Directed Research and Development Project 213034.

Sandia National Laboratories is a multimission laboratory managed and operated by National Technology and Engineering Solutions of Sandia, LLC, a wholly owned subsidiary of Honeywell International, Inc., for the U.S. Department of Energy's National Nuclear Security Administration under contract DE-NA0003525.

This paper describes objective technical results and analysis. Any subjective views or opinions that might be expressed in the paper do not necessarily represent the views of the U.S. Department of Energy or the United States Government.

REFERENCES

[1] White, Howard, Tobik, Timothy, Mabry Richard, and Beliveau, Alain. *High-G Testing for Fuze Research*, 74th Shock and Vibration Symposium, 2003.

[2] Frew, Danny, Forrestal, Michael, and Chen, Wayne. *Pulse Shaping Techniques for Testing Elastic-Plastic Materials with a Split Hopkinson Pressure Bar*, Experimental Mechanics, vol. 45, 2005.

[3] Othman, Ramzi. *The Kolsky-Hopkinson Bar Machine: Selected Topics*, 2018.

[4] DeVost,V. *VHg Impact Test Set*, United States Naval Ordnance Laboratory, 1968.

[5] Lansmont, *Model 23 Shock Test System*, https://www.lansmont.com/products/shock/standard-shock-test-systems/lansmont-23/.

[6] Curtis, Shane, White, Caleb, Dye, Joshua. *Preliminary Testing for an Ultra High-G Recoverable Data Recorder*, Sandia National Laboratories, 2021.

[7] White, Caleb, Curtis, Shane, Dye, Joshua, Davis, Taylor, Cothell, David. *Investigation of enabling technologies for an Ultra-High-G Recoverable Data Recorder*, Sandia National Laboratories, 2021.

[8] Wong, M. *CTH User's Manual Version 12.1*, 2019.

[9] Adams, Brian, Bohnhoff, William, Dalbey, Keith, Ebeida, Mohamed, Eddy, John, Eldred, Michael, Hooper, Russell, Hough, Patricia, Hu, Kenneth, Jakeman, John, Khalil, Mohammad, Maupin, Kathryn, Monschke, Jason, Ridgway, Elliott, Rushdi, Ahmad, Seidl, Daniel, Stephens, John, Winokur, Justin. *Dakota, a Multilevel Parallel Object-Oriented Framework for Design Optimization, Parameter Estimation, Uncertainty Quantification, and Sensitivity Analysis: Version 6.13 User's Manual*, 2020.

[10] McGlaun, James, Thompson, Samuel, and Elrick, Mildred. *CTH: A Three-Dimensional Shock Wave Physics Code*, International Journal of Impact Engineering, vol. 10, 1990.

[11] Skroch, Michael, Owen, Steven, Staten, Matthew, Quadros, Roshan, Hanks, Byron, Clark, Brett, Hensley, Trevor, Ernst, Corey, Morris, Randy, McBride, Corey, Stimpson, Clinton, Perry, James, Richardson, Mark, and Merkley, Karl. *Cubit 15.7 User Documentation*, 2020.

[12] Ellis, Jeremy. *The Effect of Projectile Nose Shape on the Formation of the Water Entry Cavity*, Brigham Young University, Master's Thesis, 2016.

[13] Hrubes, J. *High-Speed Imaging of Supercavitating Underwater Projectiles*, Experiments in Fluids, vol. 30, no. 1, 2001.

[14] Kim, S Seonhong and Kim, Nakwan. *Integrated Dynamics Modeling for Supercavitating Vehicle Systems*, International Journal of Naval Architecture and Ocean Engineering, vol. 7, no. 2, 2015.

[15] Truscott, T Tadd, Beal, David, and Techet, Alexandra. *Shallow Angle Water Entry of Ballistic Projectiles*, 7th International Symposium on Cavitation, 2009.

[16] White, Caleb. *Qualitative Investigation of Gaseous Hydrodynamic Mixing Model Efficacy and Associated Sensitivity*, Master's Thesis, University of New Mexico, 2020.

[17] Swiler, Laura and Wyss, Dane. *A User's Guide to Sandia's Latin Hypercube Sampling Software: LHS Unix*

Library/Standalone Version, Sandia National Laboratories, 2004.
[18] Gaberson Howard, Chalmers, R. *Modal Velocity as a Criterion of Shock Severity*, Shock and Vibration Bulletin, no. 40, part 2, Naval Research Lab, 1969.
[19] Bodie Technology, Inc. *Understanding Shock Spectra and PVSS Analysis*, Analyzing Noisy Data from Physical Tests & Transient FEA, 2021.
[20] Wolfson, Janet. *21-G-041 Fuze Modeling Grand Challenge Final Report*, Joint Fuze Technology Program, 2018.
[21] SAS Institute Inc., *JMP 16 Documentation Library*, 2021-2022.